Buckling of rectangular and hexagonal honeycomb under combined axial compression and transverse shear

F. López Jiménez [a], N. Triantafyllidis [a,b,c,*]

[a] *Laboratoire de Mécanique des Solides, UMR CNRS 7649, France*
[b] *Département de Mécanique, École Polytechnique, 91128 Palaiseau Cedex, France*
[c] *Aerospace Engineering Department and Mechanical Engineering Department (emeritus), The University of Michigan, Ann Arbor, MI 48109-2140, USA*

ABSTRACT

One of the many uses of honeycomb is as core in sandwich plates, producing very high stiffness-to-weight ratio structures. The macroscopically observed crushing mechanism of these structures has its origin in instabilities at the local scale. Of particular interest here are the critical (i.e., onset of a buckling-type instability) loads and corresponding eigenmodes of honeycomb under general 3D loading involving simultaneous axial compression and transverse shear.

Since the critical eigenmodes in honeycomb often involve more than one unit cell, numerical studies are limited by the size of the domain considered for their analyses. We propose a new theoretical approach to determine the critical loads and eigenmodes of perfect honeycomb of infinite extent under general loading conditions based entirely on unit-cell calculations. It combines Bloch wave representation theorem for the eigenmode with the analytical solution of the linearized von Kármán plate equations for the walls. The proposed approach uses the fact that the honeycomb walls remain flat in the principal solution prior to the onset of the first instability and solves analytically the corresponding eigenvalue problem. Three different geometries are considered: rectangular honeycomb with varying in-plane aspect ratios, an isotropic-section hexagonal honeycomb, and an anisotropic-section hexagonal honeycomb (resulting from its manufacturing process).

Several different loading cases are investigated: axial compression under free or fully constrained lateral expansion, transverse shear and combined axial compression and transverse shear. The results show that the buckling mode is highly dependent on the type of loading: e.g., laterally unconstrained axial compression results in local critical eigenmodes, while constraining the lateral expansion leads to global ones. The addition of transverse shear not only reduces the critical axial strain, but also affects the wavelengths of the critical eigenmode.

© 2013 Elsevier Ltd. All rights reserved.

1. Introduction

Honeycomb is a prismatic 3D structure resulting by translating a 2D periodic cellular, planar pattern along its normal direction, usually referred to as its *"axial"* direction. Their 2D unit cells are typically hexagonal but many other cell geometries have been used in applications. Their low weight-to-stiffness ratios, outstanding energy absorption characteristics and cost effectiveness make for their widespread use in technological applications (Gibson and Ashby, 1997). Applications involve compressive loading either in-plane or out-of-plane, along the axial direction, as it is typically the case of sandwich panels, where the honeycomb serves as core between two flat plates perpendicular to its axis. It is the axial loading case that is of interest here.

Failure in honeycomb, and cellular solids in general, is typically in the form of zones of localized deformation and is due to a bifurcation instability initiated at the local level; as it turns out the highly symmetric cell-periodic mode of deformation (where all cells deform identically) becomes unstable at some stress level and a bifurcation mode that breaks this symmetry appears. The emerging post-bifurcation equilibrium path shows a limit point in the global force–displacement response and hence a localization of deformation follows. Unlike the in-plane crushing of honeycomb, where this bifurcation occurs after substantial bending of the cell walls (typically in the plastic range of the material's response) (Papka and Kyriakides, 1994, 1998; Triantafyllidis and Schraad, 1998), in the case of axial crushing the first (as the load increases) bifurcation instability emerges from a principal solution where the cell walls are flat (Wilbert et al., 2011), a fact that we exploit in this work to obtain an analytical solution for the corresponding problem. From the vast literature on the crushing

---

* Corresponding author at: Département de Mécanique, École Polytechnique, 91128 Palaiseau Cedex, France. Tel.: +33 1 69 33 57 98.
E-mail address: nick@lms.polytechnique.fr (N. Triantafyllidis).

of honeycomb, in this paper we mainly refer to work pertaining to the onset of buckling instabilities of honeycomb under quasistatic loading conditions.

Realistic modeling of the axial compression of honeycomb that shows how the initial buckling mode develops into a localized deformation pattern requires large (i.e., involving many cells) numerical models, resulting in highly time consuming calculations even for in-plane simulations (Papka and Kyriakides, 1998, 1999; Okumura et al., 2002). When axial crushing is considered and 3D prismatic honeycomb models are used (Aktay et al., 2008; Wilbert et al., 2011), in addition to the question about the adequate number of unit cells one also must determine the critical wavelength in the axial direction. Simulations of experiments do take into account the size of the specimen and applied boundary conditions. However, it is important to establish the critical load and corresponding eigenmode for the infinite honeycomb, by ignoring the influence of boundary conditions.

Calculating the onset-of-instability in a perfectly periodic, finitely strained, rate-independent solid of infinite extent and thus finding the lowest critical load and corresponding mode for a given loading path relies on the Bloch wave representation theorem and requires modeling of only the smallest unit cell, as shown for the case of in-plane compression of 2D grillages (Triantafyllidis and Schnaidt, 1993), 2D honeycomb (Triantafyllidis and Schraad, 1998), 3D Kelvin foam (Gong et al., 2005) and more generally of arbitrary loading in periodic, two-phase continua (Triantafyllidis et al., 2006). Fortunately for our case, the investigations of Wilbert et al. (2011) show that, due to the symmetry of structure and loading, buckling in axially compressed honeycomb emerges from a principal solution where all cell walls are flat, thus allowing for an analytical solution to the corresponding bifurcation problem.

Following the motivation for this work in Section 1, the model is presented in Section 2 using a new theoretical approach to determine the critical loads and eigenmodes of perfect honeycomb of infinite extent under general loading conditions based entirely on calculations involving the smallest unit cell. The method combines Bloch wave representation theorem for the eigenmode with the analytical solution of the linearized von Kármán plate equations for the bi-axially compressed cell walls. The problem is formulated for three different geometries: rectangular honeycomb with varying in-plane aspect ratios, an isotropic-section hexagonal honeycomb, and a realistic anisotropic-section hexagonal honeycomb where some walls have double thickness due to its manufacturing process. The principal solution takes into account not only axial compression but also transverse shear in any orientation with respect to the cell's principal axes and the possibility of a fully constrained lateral expansion, since the corresponding state of stress and the symmetry of the perfect structure guarantee that the cell walls are in equilibrium in a configuration where all cell walls are flat and under uniform in-plane stresses. Results in Section 3 are given for the three different geometry honeycomb under several different loading scenarios: axial compression with free or fully constrained lateral expansion, transverse shear and combined axial compression and transverse shear. The results show that the buckling mode is highly dependent on the type of loading and lateral contraint conditions. The addition of transverse shear not only reduces the critical axial strain, but also affects the wavelengths of the critical eigenmode. The presentation ends with a discussion in Section 4.

2. Formulation

This section details the theoretical approach followed in the present study. Section 2.1 describes the proposed model, which combines Bloch wave representation theorem and the analytical

solution of the linearized von Kármán plate equation. Section 2.2 gives more details on the loading. Section 2.3 describes the procedure to determine the critical load and corresponding eigenmode at the onset-of-instability. As a check to our calculations, the analytical results for the loss of ellipticity of the homogenized structure are compared for the case of rectangular honeycomb with the results provided by the Bloch-wave analysis for long wavelength modes in Appendix A. A finite element model, detailed in Appendix B, is also used for another independent comparison with the model's analytical predictions and eigenmode visualization.

2.1. Model description

Three different geometries are considered: rectangular honeycomb with a varying in-plane aspect ratio, an isotropic-section hexagonal honeycomb (all plates with equal thickness) and an anisotropic-section hexagonal honeycomb (one set of plates with double thickness, corresponding to the usual manufacturing procedure that uses strips of glue on initially flat plates that are subsequently pulled apart), as shown in Fig. 1.

The proposed method deviates from the traditional approach of numerical determination of the lowest load corresponding to a local energy minimum of the principal solution. Instead, our approach makes use of the fact that the honeycomb plates remain flat in the principal solution prior to the onset of the first instability, as shown experimentally by Wilbert et al. (2011) for axially compressed Al honeycomb, and solves analytically the corresponding eigenvalue problem.

The starting point for calculating the critical load and eigenmode are the Euler–Lagrange equations resulting from vanishing of the second variation of the system's potential energy. In the experiments by Wilbert et al. (2011) the onset of instability in axially loaded thin wall honeycomb occurs in the elastic range of the wall's response, thus further simplifying our analysis, although a generalization for thick wall honeycomb requiring elasto-plastic constitutive modeling is straightforward. In each cell wall, von Kármán plate theory dictates that the partial differential equation for the out-of-plane eigenmode component w, expressed in local coordinates, is:

$$(D/t)\Delta^2 w - \sigma_{\alpha\beta} w_{,\alpha\beta} = 0, \tag{1}$$

where $D = Et^3/(12(1-v^2))$ is the bending stiffness, t is the plate thickness, E its Young modulus, v its Poisson ratio, and $\sigma_{\alpha\beta}$ is the in-plane stress of the plate. Here and subsequently Greek indexes
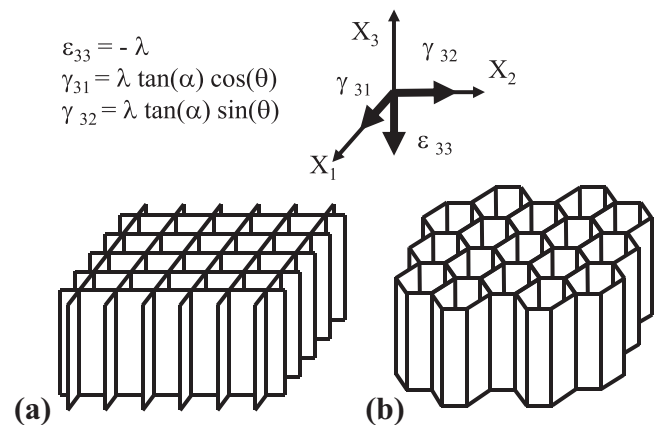

Fig. 1. Undeformed configuration of honeycomb investigated here: (a) rectangular and (b) hexagonal. Definitions of the combined compression and shear loading strains shown here are given in Eq. (15).

F. López Jiménez, N. Triantafyllidis / International Journal of Solids and Structures 50 (2013) 3934–3946

range from 1 to 2 while Latin ones from 1 to 3. Einstein's summation convention is assumed over repeated indexes.

For the in-plane eigenmode components, u_α, we have in each cell wall:

$$L_{\alpha\beta\gamma\delta}u_{\gamma,\beta\delta} = 0, \tag{2}$$

where $L_{\alpha\beta\gamma\delta}$ are the components of the plane stress moduli tensor of the plate:

$$L_{\alpha\beta\gamma\delta} = \frac{E}{1-v^2}\left(\frac{1-v}{2}\left(\delta_{\alpha\gamma}\delta_{\beta\gamma} + \delta_{\alpha\delta}\delta_{\beta\gamma}\right) + v\delta_{\alpha\beta}\delta_{\gamma\beta}\right). \tag{3}$$

The bifurcation equations (1) and (2) need to be completed with appropriate boundary conditions at cell wall boundaries of the RVE, shown for each honeycomb considered in Fig. 2. At this point we invoke the Bloch wave representation theorem for the eigenmode, according to which the eigenmode can be put in the form:

$$\mathbf{v}(X_1, X_2, X_3) = \mathbf{p}(X_1, X_2)\exp\left(i(\omega_1 X_1 + \omega_2 X_2 + \omega_3 X_3)\right), \tag{4}$$

where $\mathbf{v} \equiv (u_1, u_2, w)$, $\mathbf{p}$ is a periodic function with period the RVE and the wavenumber $\boldsymbol{\omega} \equiv (\omega_1, \omega_2, \omega_3)$ with $0 \leqslant \omega_1 L_1 \leqslant 2\pi$, $0 \leqslant \omega_2 L_2 \leqslant 2\pi$ and $\omega_3 \in \mathbb{R}$.

Thanks to the Bloch wave theorem and the invariance of the principal solution along X_3, all derivatives with respect to the axial local coordinate x_2, equivalent to the global coordinate X_3 (see Fig. 2), can be substituted as:

$$\frac{\partial f}{\partial x_2} = i\omega_3 f, \tag{5}$$

where f is a field quantity and ω_3 is the corresponding Bloch wavenumber in X_3.

Within each cell wall, and expressed in the corresponding local system, the partial differential equations transform into ordinary differential equations with respect to x_1:

$$\frac{w_{,1111}}{(\omega_3)^4} - \frac{2w_{,11}}{(\omega_3)^2} + w - \frac{\sigma_{11}w_{,11} + i\omega_3\sigma_{12}w_{,1} - (\omega_3)^2\sigma_{22}w}{(D/t)(\omega_3)^4} = 0,$$

$$u_{1,11} + i\omega_3\frac{1+v}{2}u_{2,1} - (\omega_3)^2\frac{1-v}{2}u_1 = 0, \tag{6}$$

$$\frac{1-v}{2}u_{2,11} + i\omega_3\frac{1+v}{2}u_{1,1} - (\omega_3)^2 u_2 = 0.$$

Solving the above equations yields the following expressions for w and u_α:

$$w = A_1 e^{q_1\omega_3 x_1} + A_2 e^{-q_1\omega_3 x_1} + A_3 e^{q_2\omega_3 x_1} + A_4 e^{-q_2\omega_3 x_1}$$

$$u_1 = B_1 e^{\omega_3 x_1} + B_2 e^{-\omega_3 x_1} + B_3 x_1 e^{\omega_3 x_1} + B_4 x_1 e^{-\omega_3 x_1}$$

$$u_2 = \left(B_1 + \frac{3-v}{(1+v)\omega_3}B_3\right)e^{\omega_3 x_1} + \left(-B_2 + \frac{3-v}{(1+v)\omega_3}B_4\right)e^{-\omega_3 x_1}$$
$$+ B_3 x_1 e^{\omega_3 x_1} + B_4 x_1 e^{-\omega_3 x_1} \tag{7}$$

where q_1 and q_2 can be either real or imaginary constants satisfying the equation:

$$q^4 - \left(2 + \frac{\sigma_{11}}{(D/t)(\omega_3)^2}\right)q^2 - \frac{i\sigma_{12}}{(D/t)(\omega_3)^2}q + \frac{\sigma_{22}}{(D/t)(\omega_3)^2} + 1 = 0. \tag{8}$$

The response of each cell wall has therefore 8 unknowns, which need to be determined applying appropriate boundary and periodicity conditions that depend on the honeycomb microstructure.

2.1.1. Rectangular microstructure

The rectangular RVE, of aspect ratio r, consists of four plates, see Fig. 2a, which means that a total of 32 equations are needed. These are the Bloch wave periodicity conditions, which relate the kinematics and reaction forces in opposite ends of the RVE, as well as displacement continuity and force/moment equilibrium in the
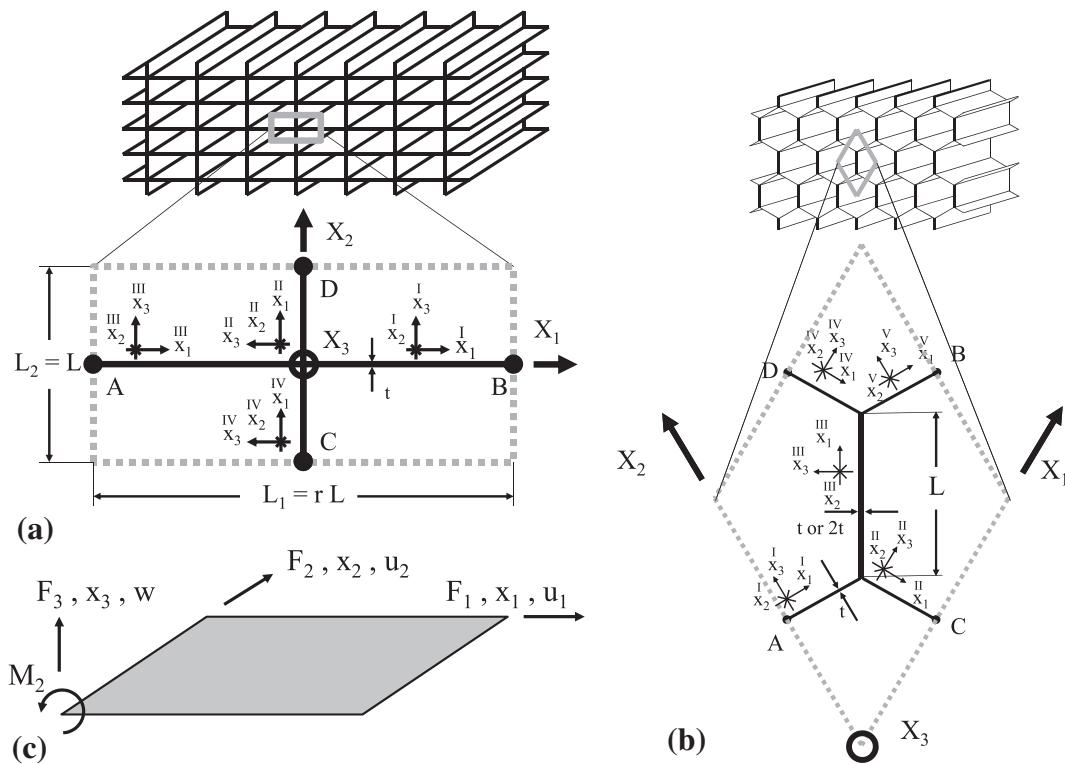

Fig. 2. Representative volume elements (RVEs) for: (a) rectangular, (b) hexagonal honeycomb, and (c) local plate coordinate system.

central nodal line. To avoid lengthy, but straightforward recordings of the equations, their summary is presented in Table 1.

Bloch wave conditions relating field equations at opposite ends with same X_i coordinate of the unit cell take the form:

$$f_B = f_A \exp(i\omega_1 L_1) \quad f_D = f_C \exp(i\omega_2 L_2), \tag{9}$$

where f_N stands for any field quantity evaluated at the node N.

The first 28 equations relate displacements or their derivatives plate by plate, while in the last four equations all the plates are involved. The derivations of the last four equations are detailed in what follows:

Equilibrium of forces in the global X_1 direction results in:

$$
-\frac{Et}{1-v^2}\left(\overset{I}{u}_{1,1} + i\omega_3 v \overset{I}{u}_2\right)
$$
$$
-\frac{Et^3}{12(1-v^2)}\left(\overset{II}{w}_{,111} - (\omega_3)^2(2-v)\overset{II}{w}_{,1}\right) + t\left(i\omega_3 \overset{II}{\sigma}_{12}\overset{II}{w} + \overset{II}{\sigma}_{11}\overset{II}{w}_{,1}\right)
$$
$$
+\frac{Et}{1-v^2}\left(\overset{III}{u}_{1,1} + i\omega_3 v \overset{III}{u}_2\right) + \frac{Et^3}{12(1-v^2)}\left(\overset{IV}{w}_{,111} - (\omega_3)^2(2-v)\overset{IV}{w}_{,1}\right)
$$
$$
- t\left(i\omega_3 \overset{IV}{\sigma}_{12}\overset{IV}{w} + \overset{IV}{\sigma}_{11}\overset{IV}{w}_{,1}\right) = 0, \tag{10}
$$

where all functions are evaluated at the central node at the onset of instability. Equivalently, for the equilibrium of forces in the global X_2 direction, one has:

$$
\frac{Et^3}{12(1-v^2)}\left(\overset{I}{w}_{,111} - (\omega_3)^2(2-v)\overset{I}{w}_{,1}\right)
$$
$$
- t\left(i\omega_3 \overset{I}{\sigma}_{12}\overset{I}{w} + \overset{I}{\sigma}_{11}\overset{I}{w}_{,1}\right) - \frac{Et}{1-v^2}\left(\overset{II}{u}_{1,1} + i\omega_3 v \overset{II}{u}_2\right)
$$
$$
- \frac{Et^3}{12(1-v^2)}\left(\overset{III}{w}_{,111} - (\omega_3)^2(2-v)\overset{III}{w}_{,1}\right) + t\left(i\omega_3 \overset{III}{\sigma}_{12}\overset{III}{w} + \overset{III}{\sigma}_{11}\overset{III}{w}_{,1}\right)
$$
$$
+ \frac{Et}{1-v^2}\left(\overset{IV}{u}_{1,1} + i\omega_3 v \overset{IV}{u}_2\right) = 0. \tag{11}
$$

Equilibrium of forces in the global X_3 direction, due to in-plane shear, yields:

$$
-\frac{E}{2(1+v)}\left(i\omega_3 \overset{I}{u}_1 + \overset{I}{u}_{2,1}\right) - \frac{E}{2(1+v)}\left(i\omega_3 \overset{II}{u}_1 + \overset{II}{u}_{2,1}\right)
$$
$$
+\frac{E}{2(1+v)}\left(i\omega_3 \overset{III}{u}_1 + \overset{III}{u}_{2,1}\right) + \frac{E}{2(1+v)}\left(i\omega_3 \overset{IV}{u}_1 + \overset{IV}{u}_{2,1}\right) = 0. \tag{12}
$$

Finally, equilibrium of moments around the global X_3 axis gives:

$$
-\frac{Et^3}{12(1-v^2)}\left(\overset{I}{w}_{,11} - (\omega_3)^2 v \overset{I}{w}\right) - \frac{Et^3}{12(1-v^2)}\left(\overset{II}{w}_{,11} - (\omega_3)^2 v \overset{II}{w}\right)
$$
$$
+\frac{Et^3}{12(1-v^2)}\left(\overset{III}{w}_{,11} - (\omega_3)^2 v \overset{III}{w}\right) + \frac{Et^3}{12(1-v^2)}\left(\overset{IV}{w}_{,11} - (\omega_3)^2 v \overset{IV}{w}\right) = 0, \tag{13}
$$

thus completing the set of incremental equilibrium equations for the central node of the rectangular honeycomb's RVE.

2.1.2. Hexagonal microstructure

The RVE used to study the hexagonal honeycomb has five plates, see Fig. 2b, and thus 40 equations are needed. Again to avoid recording lengthly but straightforward expressions their summary is presented in Table 2:

The Bloch wave conditions relating field quantities at opposite ends of the RVE are given again by (9). The force equilibrium in the global X_1 and X_2 directions now needs to take into account the angle of the plates. The contribution of the Jth plate is given by:

$$
\overset{J}{F}_1 = \left[-\frac{E\overset{J}{t}}{1-v^2}\left(\overset{J}{u}_{1,1} + i\omega_3 v \overset{J}{u}_2\right)\right]\cos\overset{J}{\theta}
$$
$$
+ \left[-\frac{E(\overset{J}{t})^3}{12(1-v^2)}\left(\overset{J}{w}_{,111} - (\omega_3)^2(2-v)\overset{J}{w}_{,1}\right) + \overset{J}{t}\left(i\omega_3 \overset{J}{\sigma}_{12}\overset{J}{w} + \overset{J}{\sigma}_{11}\overset{J}{w}_{,1}\right)\right]\sin\overset{J}{\theta},
$$
$$
\overset{J}{F}_2 = \left[-\frac{E\overset{J}{t}}{1-v^2}\left(\overset{J}{u}_{1,1} + i\omega_3 v \overset{J}{u}_2\right)\right]\sin\overset{J}{\theta}
$$
$$
+ \left[\frac{E(\overset{J}{t})^3}{12(1-v^2)}\left(\overset{J}{w}_{,111} - (\omega_3)^2(2-v)\overset{J}{w}_{,1}\right) - \overset{J}{t}\left(i\omega_3 \overset{J}{\sigma}_{12}\overset{J}{w} + \overset{J}{\sigma}_{11}\overset{J}{w}_{,1}\right)\right]\cos\overset{J}{\theta}. \tag{14}
$$

where $\overset{J}{\theta}$ is the angle of the Jth plate in the $X_1 - X_2$ plane. It should be noted that the thickness $\overset{J}{t}$ is the same for all plates in the isotropic-section honeycomb, but not for the anisotropic-section honeycomb, where $\overset{III}{t} = 2\overset{I}{t} = 2\overset{II}{t} = 2\overset{IV}{t} = 2\overset{V}{t}$.

2.2. Loading

The applied loading is a combination of axial compression (along X_3 in the global coordinate system), as well as out-of-plane shear. Two different cases are considered for the lateral expansion: either the honeycomb is free to expand laterally due to Poisson's effect, or this expansion is completely constrained. In the later case the geometry of the honeycomb in the $X_1 - X_2$ plane is fixed (i.e., no in-plane strains), which produces in-plane stresses in the cell walls.

In all cases the applied loading produces a principal solution where each cell wall (plate) is in a state of uniform in-plane stress $\sigma_{\alpha\beta}$. It is convenient to use the global strains applied to the structure to parameterize the applied loading. The applied strains on

Table 1
Summary of the eigenmode equations for the RVE of the rectangular microstructure.

Bloch wave conditions		
Plates I and III – Kinematics	u_α, w and $w_{,1}$	4 equations
Plates I and III – Forces	$u_{\alpha,\beta}$, $w_{,11}$ and $w_{,111}$	4 equations
Plates II and IV – Kinematics	u_α, w and $w_{,1}$	4 equations
Plates II and IV – Forces	$u_{\alpha,\beta}$, $w_{,11}$ and $w_{,111}$	4 equations
Kinematics at central node		
Plates I and III	u_α, w and $w_{,1}$	4 equations
Plates I and IV	u_α, w and $w_{,1}$	4 equations
Plates I and II	u_α, w and $w_{,1}$	4 equations
Equilibrium at central node		
Plates I to IV	F_1, F_2, F_3 and M_3	4 equations

Table 2
Summary of the eigenmode equations for the RVE of the hexagonal microstructure.

Bloch wave conditions		
Plates I and V – Kinematics	u_α, w and $w_{,1}$	4 equations
Plates I and V – Forces	$u_{\alpha,\beta}$, $w_{,11}$ and $w_{,111}$	4 equations
Plates II and IV – Kinematics	u_α, w and $w_{,1}$	4 equations
Plates II and IV – Forces	$u_{\alpha,\beta}$, $w_{,11}$ and $w_{,111}$	4 equations
Kinematics at central nodes		
Plates I and II	u_α, w and $w_{,1}$	4 equations
Plates I and III	u_α, w and $w_{,1}$	4 equations
Plates III and IV	u_α, w and $w_{,1}$	4 equations
Plates III and V	u_α, w and $w_{,1}$	4 equations
Equilibrium at central nodes		
Plates I to III	F_1, F_2, F_3 and M_3	4 equations
Plates III to V	F_1, F_2, F_3 and M_3	4 equations

the structure, expressed in the global coordinate system X_i, see Fig. 1, are:

$$\epsilon_{33} = -\lambda,$$
$$\gamma_{31} = \lambda \tan \alpha \, \cos \theta, \tag{15}$$
$$\gamma_{32} = \lambda \tan \alpha \, \sin \theta,$$

where $\lambda > 0$, α describes the axial to shear strain mixity, i.e., $\tan \alpha$ gives the ratio between applied axial and shear strains, and θ the shear orientation, i.e., $\tan \theta$ represents the ratio of the shear components along the X_1-X_2 directions.

The local strains at the Jth plate of a square or isotropic-section hexagonal honeycomb are:

$$\overset{J}{\epsilon}_{22} = -\lambda,$$

$$\overset{J}{\epsilon}_{11} = \begin{cases} -\nu\lambda & \text{for free lateral expansion} \\ 0 & \text{for constrained lateral expansion} \end{cases}, \tag{16}$$

$$\overset{J}{\gamma}_{12} = \lambda \tan \alpha \, \cos \left(\theta - \overset{J}{\theta} \right),$$

where $\overset{J}{\theta}$ is the angle of the plate with respect to the X_1 axis. The expression for $\overset{J}{\gamma}_{12}$ in (16) is not valid in the case of the anisotropic-section hexagonal honeycomb (with some walls of double thickness). In that case the planes initially perpendicular to X_3 will, in general, not remain plane, which introduces a new shear component, as seen in Fig. 3. For such a configuration, it can be calculated that the total local shear in the plates is equal to:

$$\overset{I}{\gamma}_{12} = \overset{V}{\gamma}_{12} = \lambda \frac{2k_1 + k_2}{4} \tan \alpha$$

$$\overset{II}{\gamma}_{12} = \overset{IV}{\gamma}_{12} = \lambda \frac{-2k_1 + 3k_2}{4} \tan \alpha \tag{17}$$

$$\overset{III}{\gamma}_{12} = \lambda \frac{2k_1 - k_2}{4} \tan \alpha$$

with $\quad k_1 \equiv \cos \left(\theta - \overset{I}{\theta} \right) + \cos \left(\theta - \overset{III}{\theta} \right) \quad$ and $\quad k_2 \equiv \cos \left(\theta - \overset{I}{\theta} \right) + \cos \left(\theta - \overset{II}{\theta} \right)$

2.3. Onset of instability

Once a loading path characterized by $\lambda \geqslant 0$ is defined by the pair (α, θ) it is possible to assemble a matrix $\mathbf{M}(\lambda; \omega_1, \omega_2, \omega_3)$, which represents the eigenvalue system of equations described in Table 1 or 2. For a fixed $\boldsymbol{\omega}$ the corresponding minimum buckling load parameter $\lambda_m(\omega_1, \omega_2, \omega_3)$ is defined as the lowest λ root of:

$$\text{Det}(\mathbf{M}(\lambda, \boldsymbol{\omega})) = 0 \quad \text{(for fixed } \boldsymbol{\omega} = (\omega_1, \omega_2, \omega_3)). \tag{18}$$

The critical load parameter λ_c is defined as the infimum of λ_m for all values of $\boldsymbol{\omega}$:

$$\lambda_c = \inf_{\boldsymbol{\omega}} \lambda_m(\boldsymbol{\omega}). \tag{19}$$

The function $\lambda_m(\boldsymbol{\omega})$ is continuous over all the frequency space except at the origin $\boldsymbol{\omega} = \mathbf{0}$, since that point corresponds to two different types of instability modes. The first type consists of all strictly periodic eigenmodes. The second case consists of eigenmodes with wavelengths much larger than the unit cell, $\boldsymbol{\omega} \rightarrow \mathbf{0}$. The presence of physically very different eigenmodes at the neighborhood of $\boldsymbol{\omega} = \mathbf{0}$ explains the possibility of a singularity of λ_m at $\boldsymbol{\omega} = \mathbf{0}$, and in case where the critical load corresponds to $\boldsymbol{\omega} \rightarrow \mathbf{0}$ the use of infimum in (19).

It has been shown (Geymonat et al., 1993) that if $\boldsymbol{\omega} = \delta\mathbf{n}$, with $\|\mathbf{n}\| = 1$, then:

$$\lim_{\delta \rightarrow 0} \lambda_m(\delta\mathbf{n}) \rightarrow \lambda_h(\mathbf{n}), \tag{20}$$

where $\lambda_h(\mathbf{n})$ is the critical load of the homogenized structure, defined as the lowest λ root of the corresponding acoustic tensor:

$$\text{Det}(\mathcal{L}_{ijkl}(\lambda)n_j n_l) = 0. \tag{21}$$

This fact can be used to check the validity of the presented approach. The homogenized incremental moduli of the structure $\mathcal{L}_{ijkl}(\lambda)$ can be derived from the incremental moduli of the unit cell, as detailed in Appendix A.

In practice, the most common procedure to find the value of λ at which $\mathbf{M}$ becomes singular is to track the smallest in absolute value eigenvalue β. The value at which $\beta = 0$ yields the critical value of the loading parameters, λ_m. However, in our case $\mathbf{M}$ is complex and not Hermitian, which introduces two difficulties. First, its eigenvalues are in general complex, and thus it is not possible to use the change in sign of the smallest eigenvalue to find the root of β. Second, the algorithms used to obtain eigenvalues in a general complex matrix are much less efficient than those available for a Hermitian matrix.

In view of the non-Hermitian nature of $\mathbf{M}$, its singular value decomposition (SVD) is currently employed. The SVD of a square matrix $\mathbf{M}$ is a factorization of the form $\mathbf{M} = \mathbf{UDV}$, where $\mathbf{U}$ and $\mathbf{V}$ are complex unitarian matrixes and $\mathbf{D}$ is a diagonal matrix with nonnegative real values, known as the singular values of $\mathbf{M}$. The matrix $\mathbf{M}$ is singular if at least one of the elements of $\mathbf{D}$ is equal to zero. In practice, the algorithm tracks the value of the smallest value of $\mathbf{D}$, and looks for values below a certain threshold, β_0. The critical loading parameters is then defined as the value of λ corresponding to the occurence of an entry d_i of $\mathbf{D}$ for which
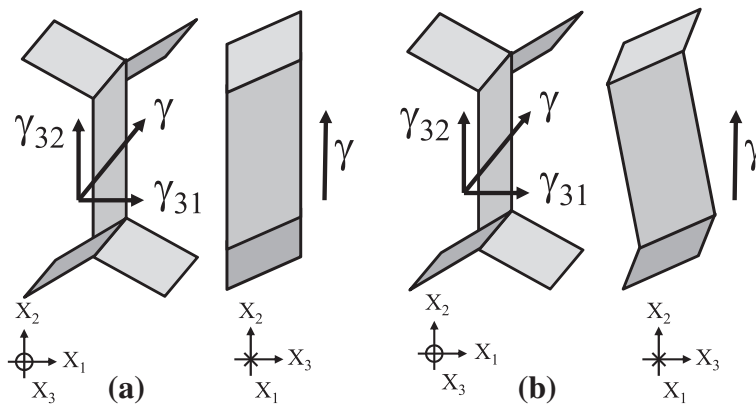

Fig. 3. Top and side view of the linearly elastic response to transverse shear for: (a) isotropic-section hexagonal RVE and (b) anisotropic-section hexagonal RVE.
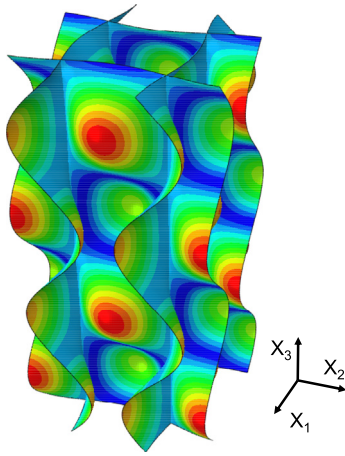
Fig. 4. Finite element calculation showing the critical mode for a square honeycomb under axial compression with free lateral expansion, with $L_3 = 4L$. The color shows the magnitude of the eigenmode displacement.

Fig. 6. Critical strain as function of aspect ratio for rectangular honeycomb under axial compression under free (solid line) or constrained (dashed line) lateral expansion.

$|d_i|_{min} \leqslant \chi |d_i|_{max}$. In the numerical calculations reported here the tolerance parameter is typically taken to be $\chi = 10^{-5}$.

A special case should be mentioned, since it affects the numerical stability of the method. It is possible for the Eq. (8) to have double roots for an specific value of λ, for which the general solution given by (7) is no longer valid. This makes **M** singular, but that does not correspond to an instability of the structure.

3. Results

In this section we will use two critical strains to plot results in a physically meaningful dimensionless way. The first one is the critical strain of a compressed infinite strip with simply supported boundary conditions:

$$\epsilon^c_{strip} = \frac{\pi^2 t^2}{3(1 - \nu^2)L^2}. \tag{22}$$

The reason for normalizing the critical load parameter in terms of ϵ^c_{strip} in (22) is the fact that this is the value of the critical strain for axial compression, $\alpha = 0$ in (15), of the rectangular honeycomb with square section and the isotropic section hexagonal honeycomb.

In the case of transverse shear without axial compression we will use the critical shear strain of an infinite strip with clamped boundary conditions (Timoshenko and Gere, 1961):
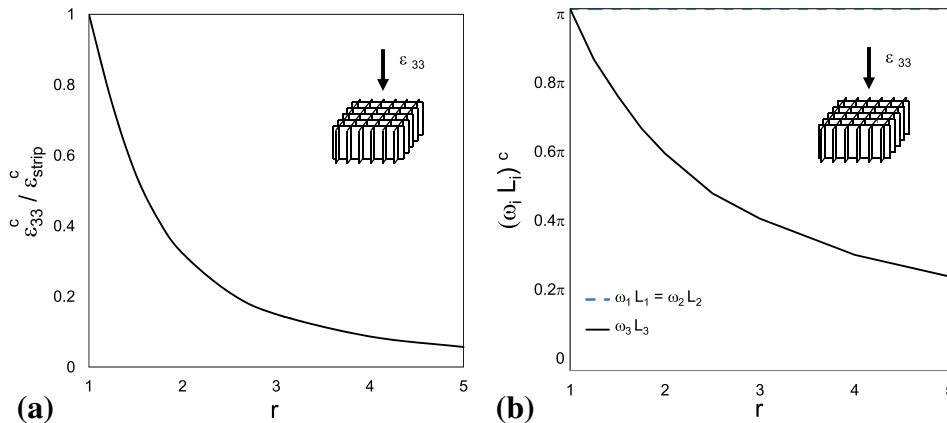
$$\gamma^c_{strip} = 1.498 \frac{\pi^2 t^2}{(1 - \nu)L^2}, \tag{23}$$

as the closest value of critical shear for the isotropic section hexagonal honeycomb, $\alpha = \pi/2$ in (15).

In all the analytical results presented here, $L_3 = L$. In numerical calculations, the value of L_3 is specified explicitly in each case.

3.1. Rectangular honeycomb

For a square honeycomb under only axial compression, allowing free lateral expansion, the critical mode corresponds to an anti-periodic mode with the same out-of-plane and in-plane wavelengths, with Bloch wave frequencies $\omega_1 L = \omega_2 L = \omega_3 L = \pi$. A finite element calculation of the mode is shown in Fig. 4. In order to obtain the correct critical buckling load, the size of the model in each dimension needs to be a multiple of the corresponding critical wavelength.

The buckling load coincides exactly with that of an infinite simply supported strip with the same thickness t and width L, given by (22). The reason is that equal rotation of all plates joined along a common line is equivalent to a simply supported boundary condition for each plate. For this reason, the results presented will be normalized by the buckling load given by (22).

If the aspect ratio $r = L_1/L_2$ increases, the critical strain becomes lower, since it is determined by the wider plate, as seen in the re-

Fig. 5. Rectangular honeycomb under axial compression with free lateral expansion: (a) critical compressive axial strain and (b) corresponding eigenmode wavenumbers as function of the aspect ratio.
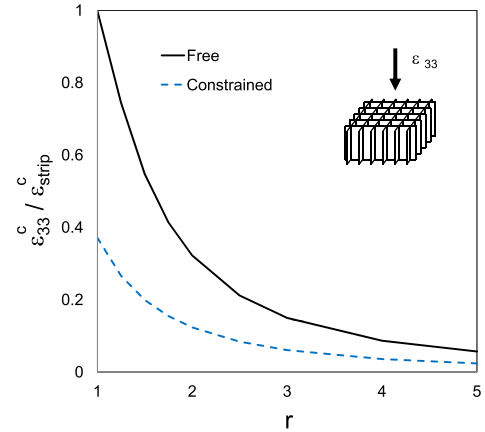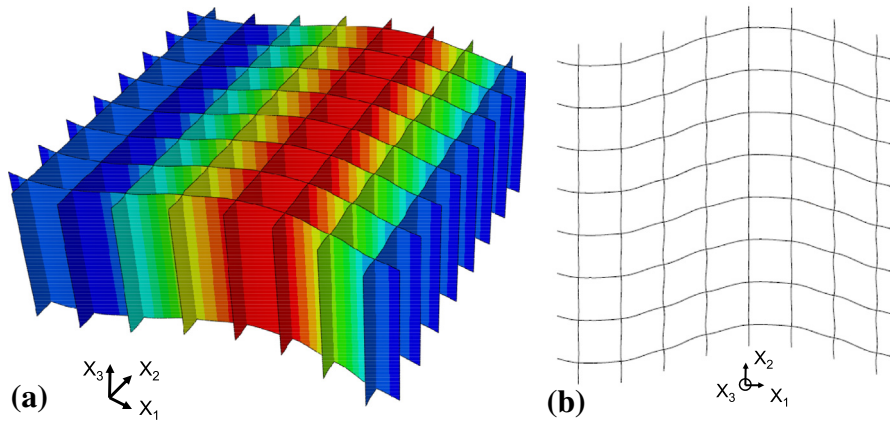
Fig. 7. Finite element calculation showing the critical mode for a square honeycomb under axial compression with constrained lateral expansion and $L_3 = 4L$: (a) axonometric and (b) top view. The X_1 wavelength of the instability is determined by the computational model size. The color shows the magnitude of the eigenmode displacement.
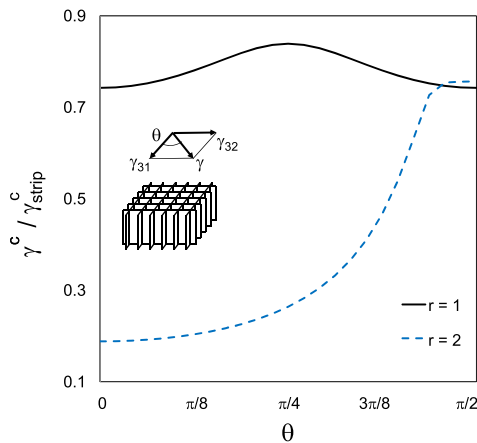

Fig. 8. Critical strain as a function of its orientation for rectangular honeycomb under transverse shear with unconstrained lateral expansion for two different aspect ratios, $r = 1$ (solid line) and $r = 2$ (dashed line).

sults plotted in Fig. 5a. The instability is still an in-plane antiperi-odic mode, $\omega_1 L_1 = \omega_2 L_2 = \pi$, but the critical out-of-plane wave-length increases with r, as shown in Fig. 5b.

If the lateral expansion is constrained, the plates also carry in-plane stress σ_{11}, due to Poisson's effect. This additional loading has two effects. First, for a given set of $(\omega_1, \omega_2, \omega_3)$, the critical strain is lower than when lateral expansion is allowed in view of the presence of the additional compressive stresses $\sigma_{11} < 0$. Second, a different instability appears. It corresponds to a long wave-length mode, with Bloch frequencies $\omega_1 = \omega_3 \to 0$ and $\omega_2 = 2\pi$. The corresponding critical buckling strains as a function of r are shown in Fig. 6, where the results for the case of free lateral expansion are also plotted for comparison. The difference between the unconstrained and constrained critical strains is maximized for $r = 1$ and decreases monotonically with increasing aspect ratio. The eigenmode for the geometry with $r = 1$ is shown in Fig. 7. It can be independently predicted from the 2D model in Triantafylli-dis and Schnaidt (1993). As expected from the general theory (Geymonat et al., 1993), the results coincide with those obtained analyzing the loss of ellipticity in the homogenized structure in Appendix A.

The effect of transverse shear loading has been studied for two different geometries, $r = 1$ and $r = 2$. Free lateral expansion is al-lowed in both cases. The results for only shear loading are shown in Fig. 8, normalized by the critical load for the infinite strip in (23).

In this case the critical load of the honeycomb is lower than that of the infinite strip, the reason being that the joints between the plates rotate, as opposed to the clamped plate boundaries assumed in the derivation of γ^c_{strip} in (23). For the case of a square section honeycomb ($r = 1$) the critical strain graph is symmetric about $\theta = \pi/4$, in view of symmetry of the cross-section (solid line in Fig. 8). As the aspect ratio increases, the symmetry of the graph about $\theta = \pi/4$ is destroyed.
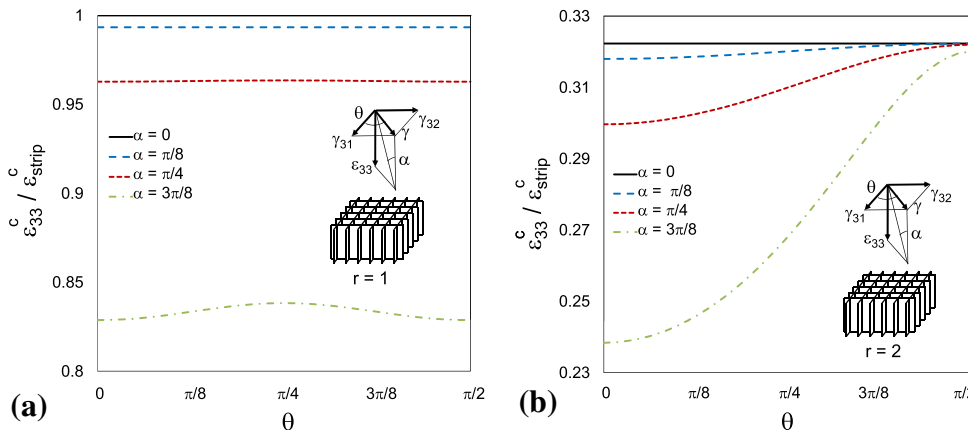

Fig. 9. Critical axial strain as a function of the shear orientation under combined compression and shear for: (a) square honeycomb, $r = 1$ and (b) rectangular honeycomb, $r = 2$.
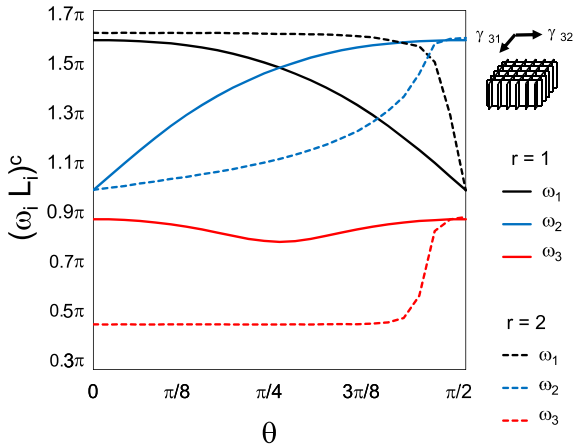
Fig. 10. Critical eigenmodes for square, $r = 1$ (solid lines) and rectangular, $r = 2$ (dashed lines) honeycomb under transverse shear as a function of the shear orientation.
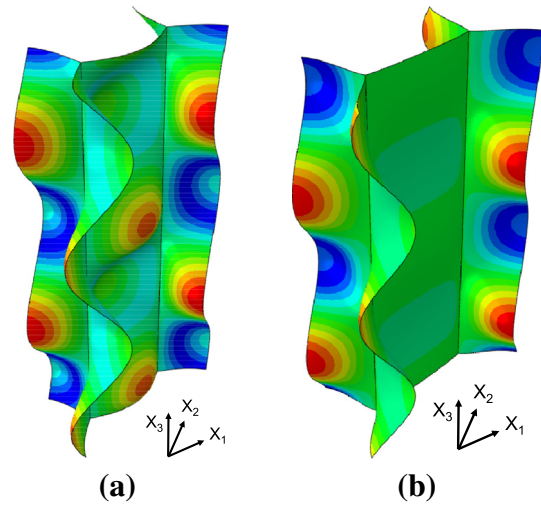

Fig. 12. Finite element calculation showing the critical mode for (a) isotropic-section hexagonal honeycomb with $L_3 = 4L$ and (b) anisotropic-section hexagonal honeycomb with $L_3 = 3.17L$ under axial compression with free lateral expansion. The color shows the magnitude of the eigenmode displacement.

In the case of combined axial compression and transverse shear, the presence of shear further destabilizes the cell walls and hence decreases the critical axial strain, as seen in Fig. 9. Note from Fig. 9a that for the square section $r = 1$, the critical axial strain is insensitive to the shear orientation θ up to significant values of the axial-to-shear strain mixity $\alpha = \pi/4$, while for the rectangular section with $r = 2$ in Fig. 9b, the critical axial strain is a monotonically changing function of both the shear orientation θ and the axial-to-shear strain mixity α.

The critical wavenumbers corresponding to the transverse shear loading reported in Fig. 8 are shown in Fig. 10. For both aspect ratios the critical eigenmodes are local, but no longer antiperiodic $\omega_1 L_1 = \omega_2 L_2 = \pi$. The values of ω_1 and ω_2 are symmetric with respect to $\pi/4$, as expected from the symmetry of the square section $r = 1$, while ω_3 is rather insensitive to the value of θ. In the case of $r = 2$ there is a clear transition in modes when the applied shear aligns to the direction of the short plate, $\theta = \pi/2$.

The eigenmodes for combined axial compression and transverse shear are shown in Fig. 11. The values of ω_1 and ω_2 increase and become more sensitive to θ as α increases. The values of ω_3 are insensitive to θ, and decrease slightly as the axial-to-shear strain mixity α increases.

The critical load and eigenmode calculations reported above for the rectangular section honeycomb will be repeated below for its hexagonal section counterpart.

3.2. Hexagonal honeycomb

The critical strain for the axially compressed, isotropic-section hexagonal honeycomb under unconstrained expansion is $\epsilon_{33}^c = \epsilon_{strip}^c$, i.e., it is equal to that of a simply supported plate of

the same width, given by (22) and hence $\omega_3 L = \pi$. The reason is the same as in the square section honeycomb: equal rotation of the plates joined along a common line results in zero bending moment, which is equivalent to simply supported boundary conditions. Due to the hexagonal cell geometry – the global axes X_1 and X_2 are no longer perpendicular – the mode is in-plane periodic, with $\omega_1 L_1 = \omega_2 L_2 = 2\pi$. The FEM-calculated critical mode is plotted in Fig. 12a.

The axially compressed, anisotropic-section honeycomb under free lateral expansion has a higher critical strain, $\epsilon_{33}^c = 1.55\epsilon_{strip}^c$ due to the presence of the double thickness cell wall. The critical eigenmode frequencies found for the infinite, perfect, anisotropic-section hexagonal honeycomb are $\omega_1 L_1 = \omega_2 L_2 = 2\pi$ and $\omega_3 L = 1.26\pi$ and the corresponding FEM-calculated critical mode is plotted in Fig. 12b. A direct comparison to experimental results is not meaningful, given the effect of finite size and boundary conditions. Nevertheless, numerical simulations of experiments in Wilbert et al. (2011) taking into account these effects show that buckling initiation takes place at $\epsilon_{33}^c \approx 1.5\epsilon_{strip}^c$, which is very close to our analytical prediction.

The case of axial compression with constrained lateral expansion can only been studied for the isotropic-section honeycomb. The current method cannot be used for the laterally constrained anisotropic-section honeycomb since in-plane equilibrium imposes bending of the cell walls in the principal solution, thus prohibiting the use of (1), the cornerstone of our analytical model presented in Section 2.1. The effect of constraining the lateral expansion for the axially compressed, isotropic-section honey-
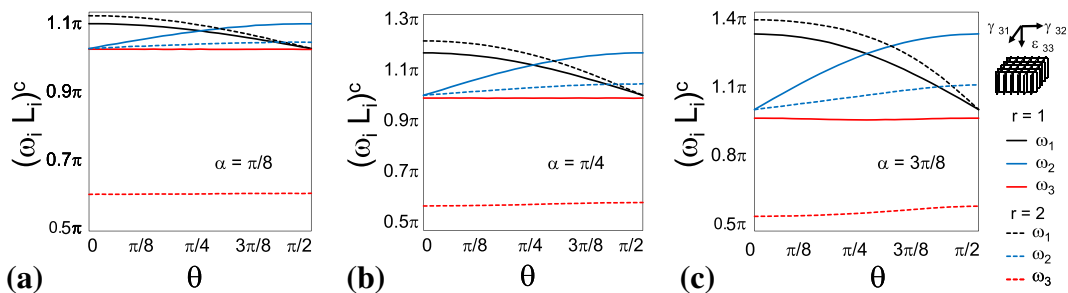

Fig. 11. Critical eigenmodes for square, $r = 1$ (solid lines) and rectangular, $r = 2$ (dashed lines) honeycomb under combined axial compression and transverse shear, as a function of the shear orientation for three different values of the axial-to-shear strain mixity: (a) $\alpha = \pi/8$, (b) $\alpha = \pi/4$ and (c) $\alpha = 3\pi/8$.
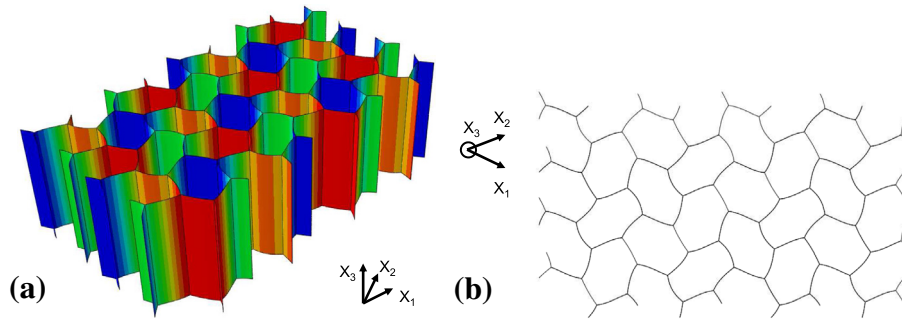
Fig. 13. Finite element calculation showing the critical mode for isotropic-section hexagonal honeycomb under axial compression with constrained lateral expansion and $L_3 = 4L$: (a) isometric and (b) top view of one of the three equivalent nodes resulting by a $\pi/3$, $2\pi/3$ rotation about X_3. The color shows the magnitude of the eigenmode displacement.
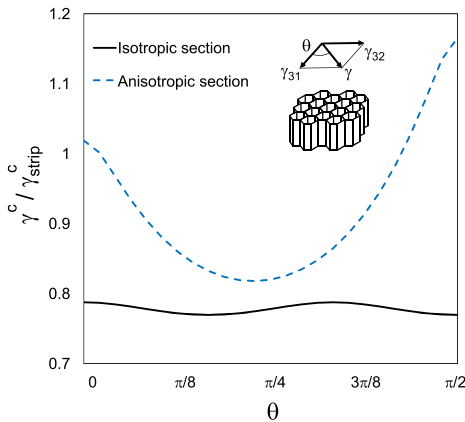

Fig. 14. Critical strain as a function of its orientation for isotropic-section (solid line) and anisotropic-section (dashed line) hexagonal honeycomb under transverse shear.

comb is similar to that on its rectangular counterpart: due to the additional compressive stresses σ_{11}, the critical strains are reduced and a long wavelength mode appears in X_3, as depicted in Fig. 13a.

The critical strain is $\epsilon_{33}^c = 0.2497\epsilon_{strip}^c$, and there are three possible critical eigenmode wavenumbers, $(\omega_1 L_1, \omega_2 L_2) = (\pi, \pi)$, $(\omega_1, L_1, \omega_2 L_2) = (\pi, 2\pi)$ and $(\omega_1 L_1, \omega_2 L_2) = (2\pi, \pi)$, which are related by a rotation of $\pi/3$ radians, due to the symmetry in the structure. This is better understood if one takes into account that, in addition to the axis X_1 and X_2, which are perpendicular to plates

I and V and plates II and IV, respectively, it is also possible to consider an axis perpendicular to plate III. The critical eigenmode wavenumber in that axis is uniquely determined by ω_1 and ω_2, such that $\omega_1 L_1 = \omega_2 L_2 = \pi$ yields a value of 2π and the other two combinations a value of π. The critical modes correspond therefore to the three possible combinations of π, π and 2π for the in-plane critical eigenmode wavenumbers. The top view of one of these eigenmodes in shown Fig. 13b.

The critical strain under transverse shear as function of the shear orientation is shown for the isotropic-section hexagonal honeycomb (solid line) and the anisotropic-section hexagonal honeycomb (dashed line) in Fig. 14. Notice that for the isotropic-section honeycomb the critical strain is rather insensitive to the load angle θ, with a maximum difference of the order of about 2.5%, while for the anisotropic-section honeycomb the corresponding difference is about 40%, with the lowest critical shear strain appearing near $\theta = \pi/6$. As expected from the existence of double thickness walls, the critical strain for the anisotropic-section honeycomb is always higher than for its isotropic-section counterpart.

For combined axial compression and transverse shear, there is again a reduction in the critical axial load, as found for the rectangular honeycomb case. Results of four different axial to shear mixity angles $\alpha = 0$, $\pi/8$, $\pi/4$, $3\pi/8$ have been calculated both for the isotropic-section case in Fig. 15a and the anisotropic-section case in Fig. 15b. Results are analogous to the ones reported for the rectangular case in Fig. 9. The critical axial strain of the isotropic-section hexagonal honeycomb decreases with increasing axial-to-shear strain mixity but is independent on the shear orientation angle θ. The corresponding values for the anisotropic-section hexagonal
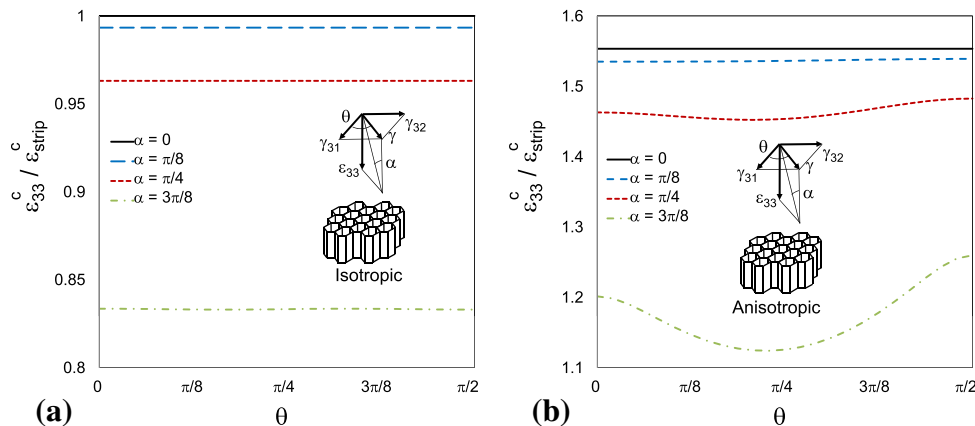

Fig. 15. Critical axial strain under combined axial compression and transverse shear as a function of the shear orientation, for different values of the axial-to-shear strain mixity, for: (a) isotropic-section hexagonal honeycomb and (b) anisotropic-section hexagonal honeycomb.
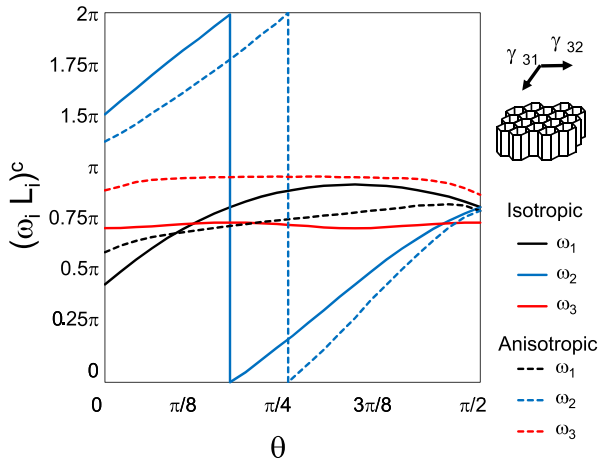
Fig. 16. Critical eigenmodes under transverse shear as a function of the shear orientation for isotropic-section hexagonal honeycomb (solid lines) and anisotropic-section hexagonal honeycomb (dashed lines).

honeycomb are consistently higher than their isotropic-section counterparts and as the axial-to-shear mixity increases are progressively more dependent on the shear orientation angle θ.

The critical mode wavenumbers for transverse shear as function of shear orientation are shown in Fig. 16 for both the isotropic-section (solid line) and anisotropic-section (dashed line) hexagonal honeycomb. Notice that the axial wavenumber ω_3 is practically insensitive to the shear orientation for both types of honeycomb, while the in-plane wavenumbers (ω_1, ω_2) show more variability.

As in the case of rectangular honeycomb in Fig. 11, the critical mode wavenumbers for combined compression and shear are plotted in terms of the shear orientation in Fig. 17. As expected, for the low axial-to-shear strain mixity the wavenumbers are insensitive to the shear orientation, but as the mixity increases they show a stronger dependence on the shear orientation, approaching the transverse shear case results in Fig. 16.

All the results reported here pertain to the lowest critical strain and associated eigenmode for a perfect rectangular and hexagonal section honeycomb of infinite extent, calculated for an elastic constitutive response of the cell walls. How the onset of the bifurcation leads to the actual failure mode by localization of deformation due to plasticity requires a more involved analysis beyond the scope of the present work.

3.3. Validity of thin-plate approximation

All calculations in this work are based on a thin plate (von Kármán theory) assumption as discussed in Section 2. In order to check the range of validity of the thin-plate approximation, a series of Bloch wave theory calculations, based on a nonlinearly elastic,
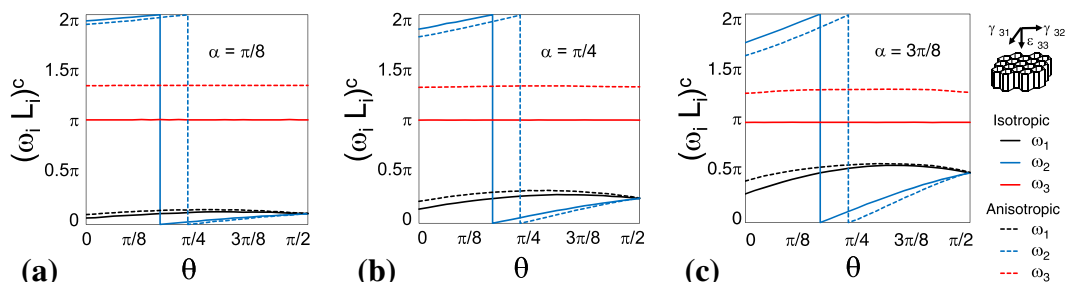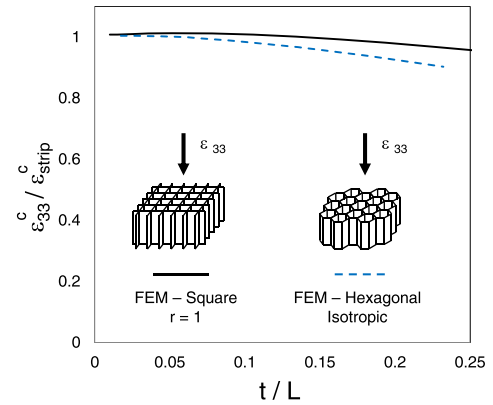

Fig. 18. Influence of wall thickness on the critical strain under axial compression, based on a full 3D simulation, for a square (solid line) and an isotropic-section hexagonal (dashed line) honeycomb. The 2D von Kármán model predictions are insensitive to wall thickness.

3D unit cell with same Young modulus and Poisson ratio have been performed on square and isotropic-section hexagonal honeycomb under axial compression and unconstrained lateral expansion. The following compressible neo-Hookean constitutive model has been used for the cell walls:

$$W = \frac{\mu}{2}[(I-3) - 3\ln J] + \frac{\kappa}{2}(J-1)^2; \ I \equiv F_{ij}F_{ij}, \ J \equiv \det(F_{ij}), \ F_{ij} = \frac{\partial x_i}{\partial X_j} \quad (24)$$

where μ and κ are, respectively, the shear and bulk moduli of the solid at zero strain. The details of the corresponding continuum, 3D calculation are given in Michel (in preparation). The exact 3D and approximate 2D critical strain predictions are indistinguishable for the square section honeycomb with $t/L < 0.1$, while the isotropic-section hexagonal honeycomb predictions start diverging for $t/L > 0.05$ as seen in Fig. 18. Since in the experiments of Wilbert et al. (2011) the cell walls were $t/L = 0.0173$, the use of the 2D von Kármán model in our onset of bifurcation calculations and of the hyperelastic constitutive model in (24) for the 3D checks are entirely appropriate for the onset of bifurcation modeling of thin walled honeycomb.

4. Conclusions

The present work pertains to the onset of a bifurcation (buckling type) instability in axially compressed and transversally sheared perfectly periodic honeycomb of infinite extent. The critical load and corresponding eigenmodes are found analytically using a Bloch wave representation of the eigenmode by considering only the smallest unit cell for different rectangular and hexagonal geometries, since they are the most frequently used in applications.

Fig. 17. Critical eigenmodes for isotropic-section (solid lines) and anisotropic-section (dashed lines) hexagonal honeycomb under combined axial compression and transverse shear, as a function of the shear orientation for three different axial-to-shear strain mixity: (a) $\alpha = \pi/8$, (b) $\alpha = \pi/4$ and (c) $\alpha = 3\pi/8$.

Due to the symmetry of loading and geometry, all cell walls remain flat in the principal solution of the 3D problem at hand. Thus the onset-of-failure mechanism is fundamentally different from the one for the in-plane crushing of honeycomb, where the destabilizing bifurcation emerges from a principal solution involving significant bending of the cell walls. Given the experimental results in axially compressed thin wall honeycomb by Wilbert et al. (2011), all calculations reported here are done in the elastic regime of the cell wall's response, although a generalization to the case of thick wall honeycomb that requires plastic constitutive description is straightforward and easily fits the framework of the present model.

For the in-plane loading, the bifurcation point is usually close to the limit load (Triantafyllidis and Schraad, 1998) but even when a limit load does not exist (Papka and Kyriakides, 1994), a subcritical bifurcated equilibrium path does provide a maximum load which finally leads to localization. Consequently for the in-plane crushing of honeycomb one can have an upper bound for the critical load of an actual, imperfect, finite-size structure by looking at its perfect counterpart of infinite extent (Triantafyllidis and Schraad, 1998).

Simulations for the bifurcation equilibrium in axially crushed honeycomb (Wilbert et al., 2011) show a stable, supercritical post-bifurcation equilibrium path that requires additional straining before reaching a maximum load that appears after the cell wall material enters the plastic range of its material response. Consequently, and in contrast with the in-plane crushing, the onset-of-bifurcation results presented here are expected to be lower bounds for the critical loads of an actual, imperfect, finite-size structure.

The main contribution of this work is, in addition to the evaluation of a lower bound for the critical load, a consistent calculation of the corresponding eigenmode for the infinite, perfect honeycomb, thus providing an estimate of a minimum representative volume needed for numerical calculations in crushing simulations. It is worth pointing out that the critical eigenmode depends strongly on the applied load orientation, as expected from past work (Triantafyllidis and Schraad, 1998; Papka and Kyriakides, 1999; Gong et al., 2005). It should also be mentioned at this point that in technological applications the plateau for the crushing is of paramount importance, but unlike the the onset of bifurcation its calculation requires the evaluation of a complicated post-bifurcated equilibrium path where plasticity, contact, friction and imperfections play a determinant role, thus adding to the appeal of the – relatively much easier – onset-of-bifurcation calculations presented here.

All the above work pertains to quasistatic loading conditions; however the use of honeycomb in shock mitigation is a very important technological application of these materials (Zhao and Gary, 1998; Yamashita and Gotoh, 2005; Rahtbun et al., 2006; Radford et al., 2007); it is worth investigating the onset of instability in honeycomb under dynamic loading conditions to determine the role of inertia on the critical load and corresponding eigenmode. Another important feature of honeycomb is the presence of adhesives, which are necessary for their manufacturing and which are sensitive to temperature thus altering the failure mode of crushed honeycomb at higher temperatures. Both topics are currently under investigation by the authors to better understand the very complex phenomena associated with the onset-of-failure mechanisms in honeycomb.

Acknowledgement

in some sense complements a part of the excellent recent work of the group of Prof. Kyriakides, by providing a theoretical complement, as well as a generalization to several more geometries and loadings, to the numerical calculations in Wilbert et al. (2011) investigating the stability of different size cell specimens. The second author had many discussions over the years with Prof. Kyriakides about the importance of a consistent, fully three-dimensional, stability analysis for cellular solids under axial loading and he is thus delighted to dedicate this paper to Prof. S. Kyriakides for his recent 60th birthday.

Appendix A. Long wavelength critical eigenmode calculation

According to the discussion following (19), $\lambda_m(\boldsymbol{\omega})$ has a singular point in the neighborhood of $\boldsymbol{\omega} = \mathbf{0}$, since the neighborhood of this point contains two physically distinct eigenmodes: the strictly periodic ones with $\boldsymbol{\omega} = \mathbf{0}$ and the eigenmodes with wavelengths much larger than the unit cell, $\boldsymbol{\omega} \to \mathbf{0}$. Fortunately, the lowest root of (18), for the case $\boldsymbol{\omega} \to \mathbf{0}$, can be found analytically by calculating the loss of ellipticity of the periodic structure's homogenized incremental moduli, as shown by Geymonat et al. (1993). This remarkable property of infinite, periodic structures will be used as a nontrivial check to ensure the validity of our calculations. For simplicity, the method is applied only to rectangular honeycomb.

The homogenized incremental moduli $\mathcal{L}_{ijkl}(\lambda)$ of the principal solution at a state characterized by the load parameter λ of a three-dimensional structure with periodic unit cell Y, can be calculated from the point-wise incremental moduli of the unit cell $L_{ijkl}(\mathbf{x}, \lambda)$ by:

$$\mathcal{L}_{ijkl}(\lambda) = \frac{1}{|Y|} \int_Y L_{mnpq}(\mathbf{x}, \lambda)\left(\delta_{im}\delta_{jn} + \chi_{m,n}^{(ij)}\right)\left(\delta_{kp}\delta_{lq} + \chi_{p,q}^{(kl)}\right) dx_1 dx_2 dx_3, \quad \text{(A.1)}$$

where $\boldsymbol{\chi}^{(ij)}(\mathbf{x})$ is the fluctuation (i.e., in excess of uniform strain) response of the unit cell to an average deformation $F_{kl}^{(ij)} = \delta_{ik}\delta_{jl}$ of the unit cell. This response can be obtained from the following variational statement:

$$\int_Y L_{mnpq}(\mathbf{x}, \lambda)\left(\delta_{kp}\delta_{lq} + \chi_{p,q}^{(kl)}\right)\delta\chi_{m,n} dx_1 dx_2 dx_3 = 0, \quad \text{(A.2)}$$

which holds for all possible Y-periodic functions $\delta\boldsymbol{\chi}(\mathbf{x})$. This procedure has been used to calculate long wavelength instabilities in two-dimensional composites (Triantafyllidis and Schnaidt, 1993), porous elastomers (Michel et al., 2007) and fiber-reinforced elastomers (Michel et al., 2010).

For the problem at hand, the principal solution, homogenized incremental moduli of the unit cell can be expressed as a function of the plane stress elastic moduli $L_{\alpha\beta\gamma\delta}$ of the plates, given in (2), as:

$$\mathcal{L}_{ijkl}(\lambda) = \frac{1}{L_1 L_2 L_3} \sum_{J=I}^{IV} \int_{A_J} \left(L_{\alpha\beta\gamma\delta}\left(\overset{(ij)}{u}_{\alpha,\beta}\overset{(kl)}{u}_{\gamma,\delta} + \frac{t^2}{12}\overset{(ij)}{w}_{,\alpha\beta}\overset{(kl)}{w}_{,\gamma\delta} \right) + \sigma_{\alpha\beta}\overset{(ij)}{w}_{,\alpha}\overset{(kl)}{w}_{,\beta} \right) t\, dx_1 dx_2,$$

$$\text{(A.3)}$$

where A_J is the area of the Jth plate, $A_J = L_J L_3$, L_3 is an arbitrary length in the X_3 direction, and the functions $\boldsymbol{\chi}^{(ij)}(\mathbf{x}) = (\overset{J^{(ij)}}{u}_1(\mathbf{x}), \overset{J^{(ij)}}{u}_2(\mathbf{x}), \overset{J^{(ij)}}{w}(\mathbf{x})); \ J = I, \ldots, IV$ are obtained from the variational statement:

$$\sum_{J=I}^{IV} \int_{A_J} \left(L_{\alpha\beta\gamma\delta}\left(\overset{J^{(ij)}}{u}_{\alpha,\beta}\delta\overset{J}{u}_{\gamma,\delta} + \frac{t^2}{12}\overset{J^{(ij)}}{w}_{,\alpha\beta}\delta_{,\gamma\delta}\overset{J}{w} \right) + \sigma_{\alpha\beta}\overset{J^{(ij)}}{w}_{,\alpha}\delta\overset{J}{w}_{,\beta} \right) dx_1 dx_2 = 0, \quad \text{(A.4)}$$

that holds for all Y-periodic functions $\delta\boldsymbol{\chi}(\mathbf{x}) = (\delta\overset{J}{u}_1(\mathbf{x}), \delta\overset{J}{u}_2(\mathbf{x}), \delta\overset{J}{w}(\mathbf{x})); \ J = I, \ldots, IV$.

Taking into account that, due to symmetry, $\partial f/\partial x_2 = 0$ for every plate, (A.4) yields the following differential equations:

$$(D/t)\,\overset{J^{(ij)}}{w}_{,1111} - \sigma_{11}\,\overset{J^{(ij)}}{w}_{,11} = 0,$$

$$\overset{J^{(ij)}}{u}_{1,11} = 0, \tag{A.5}$$

$$\overset{J^{(ij)}}{u}_{2,11} = 0.$$

Due to the additional in-plane symmetry of the unit cell, it suffices to solve for plates I and II, with the displacements depending only on the local coordinate x_1. The response for all possible modes $\left(\overset{J^{(ij)}}{u}_1(\mathbf{x}), \overset{J^{(ij)}}{u}_2(\mathbf{x}), \overset{J^{(ij)}}{w}(\mathbf{x})\right)$ are in the case when $\sigma_{11} = 0$:

$$\overset{I^{(11)}}{u}_1 = x, \quad \overset{I^{(11)}}{u}_2 = 0, \quad \overset{I^{(11)}}{w} = 0, \quad \overset{II^{(11)}}{u}_1 = 0, \quad \overset{II^{(11)}}{u}_2 = 0, \quad \overset{II^{(11)}}{w} = 0,$$

$$\overset{I^{(22)}}{u}_1 = 0, \quad \overset{I^{(22)}}{u}_2 = 0, \quad \overset{I^{(22)}}{w} = 0, \quad \overset{II^{(22)}}{u}_1 = x, \quad \overset{II^{(22)}}{u}_2 = 0, \quad \overset{II^{(22)}}{w} = 0,$$

$$\overset{I^{(33)}}{u}_1 = 0, \quad \overset{I^{(33)}}{u}_2 = y, \quad \overset{I^{(33)}}{w} = 0, \quad \overset{II^{(33)}}{u}_1 = 0, \quad \overset{II^{(33)}}{u}_2 = y, \quad \overset{II^{(33)}}{w} = 0,$$

$$\overset{I^{(13)}}{u}_1 = y, \quad \overset{I^{(13)}}{u}_2 = 0, \quad \overset{I^{(13)}}{w} = 0, \quad \overset{II^{(13)}}{u}_1 = 0, \quad \overset{II^{(13)}}{u}_2 = 0, \quad \overset{II^{(13)}}{w} = -y,$$

$$\overset{I^{(23)}}{u}_1 = 0, \quad \overset{I^{(23)}}{u}_2 = 0, \quad \overset{I^{(23)}}{w} = y, \quad \overset{II^{(23)}}{u}_1 = y, \quad \overset{II^{(23)}}{u}_2 = 0, \quad \overset{II^{(23)}}{w} = 0,$$

$$\overset{I^{(31)}}{u}_1 = 0, \quad \overset{I^{(31)}}{u}_2 = x, \quad \overset{I^{(31)}}{w} = 0, \quad \overset{II^{(31)}}{u}_1 = 0, \quad \overset{II^{(31)}}{u}_2 = 0, \quad \overset{II^{(31)}}{w} = 0,$$

$$\overset{I^{(32)}}{u}_1 = 0, \quad \overset{I^{(32)}}{u}_2 = 0, \quad \overset{I^{(32)}}{w} = 0, \quad \overset{II^{(32)}}{u}_1 = 0, \quad \overset{II^{(32)}}{u}_2 = x, \quad \overset{II^{(32)}}{w} = 0,$$

$$\overset{I^{(12)}}{u}_1 = 0, \quad \overset{I^{(12)}}{u}_2 = 0, \quad \overset{II^{(12)}}{u}_1 = 0, \quad \overset{II^{(11)}}{u}_2 = 0,$$

$$\overset{I^{(12)}}{w} = \frac{-(L_1)^2}{L_1 + L_2}\left(\frac{x}{L_1} - \frac{3x^2}{(L_1)^2} + \frac{2x^3}{(L_1)^3}\right),$$

$$\overset{II^{(12)}}{w} = \frac{(L_2)^2}{L_1 + L_2}\left(\frac{x}{L_2} - \frac{3x^2}{(L_2)^2} + \frac{2x^3}{(L_2)^3}\right) + x, \tag{A.6}$$

$$\overset{I^{(21)}}{u}_1 = 0, \quad \overset{I^{(21)}}{u}_2 = 0, \quad \overset{II^{(21)}}{u}_1 = 0, \quad \overset{II^{(21)}}{u}_2 = 0,$$

$$\overset{I^{(21)}}{w} = \frac{-(L_1)^2}{L_1 + L_2}\left(\frac{x}{L_1} - \frac{3x^2}{(L_1)^2} + \frac{2x^3}{(L_1)^3}\right) + x,$$

$$\overset{II^{(21)}}{w} = \frac{(L_2)^2}{L_1 + L_2}\left(\frac{x}{L_2} - \frac{3x^2}{(L_2)^2} + \frac{2x^3}{(L_2)^3}\right).$$

When $\sigma_{11} \neq 0$ the only terms that change are:

$$\overset{I^{(12)}}{w} = \frac{1}{\Gamma}\left(\frac{\sin\beta x}{\tan\beta L_1/2} - \cos\beta x - \frac{2x}{L_1} + 1\right),$$

$$\overset{II^{(12)}}{w} = \frac{1}{\Gamma}\left(\frac{-\sin\beta x}{\tan\beta L_2/2} + \cos\beta x + \frac{2x}{L_2} - 1\right) - x,$$

$$\overset{I^{(21)}}{w} = \frac{1}{\Gamma}\left(\frac{\sin\beta x}{\tan\beta L_2/2} - \cos\beta x - \frac{2x}{L_2} + 1\right) + x, \tag{A.7}$$

$$\overset{II^{(21)}}{w} = \frac{1}{\Gamma}\left(\frac{-\sin\beta x}{\tan\beta L_1/2} + \cos\beta x + \frac{2x}{L_1} - 1\right),$$

where $\beta = \sqrt{-t\sigma_{11}/D}$ and

$$\Gamma = \frac{2}{L_1} + \frac{2}{L_2} - \frac{\beta}{\tan\beta L_1/2} - \frac{\beta}{\tan\beta L_2/2}. \tag{A.8}$$

The corresponding values of $\mathcal{L}_{ijkl}(\lambda)$ for $\sigma_{11} = 0$ are:

$$\mathcal{L}_{1111} = \frac{Et}{(1-\nu^2)L_2}, \quad \mathcal{L}_{2222} = \frac{Et}{(1-\nu^2)L_1}, \quad \mathcal{L}_{3333} = \frac{Et(L_1+L_2)}{(1-\nu^2)L_1 L_2},$$

$$\mathcal{L}_{1313} = \frac{Et}{2(1+\nu)L_2} + \frac{\sigma_{22}t}{L_1}, \quad \mathcal{L}_{3131} = \mathcal{L}_{1331} = \mathcal{L}_{3113} = \frac{Et}{2(1+\nu)L_2},$$

$$\mathcal{L}_{2323} = \frac{Et}{2(1+\nu)L_1} + \frac{\sigma_{22}t}{L_2}, \quad \mathcal{L}_{3232} = \mathcal{L}_{2332} = \mathcal{L}_{3223} = \frac{Et}{2(1+\nu)L_1},$$

$$\mathcal{L}_{1212} = \mathcal{L}_{2121} = \mathcal{L}_{1221} = \mathcal{L}_{2112} = \frac{Et^3}{L_1 L_2(L_1+L_2)(1-\nu^2)}. \tag{A.9}$$
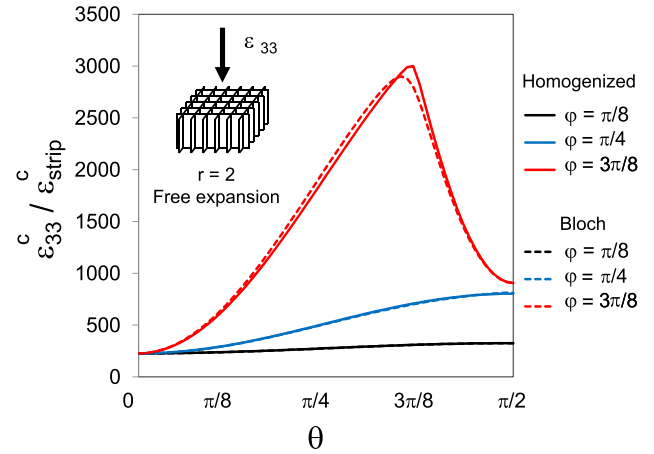

Fig. A.1. Critical buckling strain calculated by Bloch wave analysis (dashed line) and by loss of ellipticity (solid line) of the homogenized moduli of an $r = 2$ rectangular section composite with unconstrained lateral expansion.

When $\sigma_{11} \neq 0$ the terms that change are:

$$\mathcal{L}_{1111} = \frac{Et}{L_2}, \quad \mathcal{L}_{2222} = \frac{Et}{L_1}, \quad \mathcal{L}_{3333} = \frac{Et(L_1+L_2)}{L_1 L_2},$$

$$\mathcal{L}_{1212} = \sigma_{11}\left(\frac{1}{L_1} - \frac{2}{\Gamma L_1 L_2}\right), \quad \mathcal{L}_{2121} = \sigma_{11}\left(\frac{1}{L_2} - \frac{2}{\Gamma L_1 L_2}\right), \tag{A.10}$$

$$\mathcal{L}_{1221} = \mathcal{L}_{2112} = \frac{-2\sigma_{11}}{\Gamma L_1 L_2}.$$

According to (21), the loss of ellipticity occurs at the lowest λ root of:

$$\text{Det}\left(\mathcal{L}_{ijkl}(\lambda)\,n_j\,n_l\right) = 0, \tag{A.11}$$

for some unit vector $\mathbf{n}$. It is convenient to parameterize this vector as:

$$n_1 = \sin(\phi)\cos(\theta), \quad n_2 = \sin(\phi)\sin(\theta), \quad n_3 = \cos(\phi). \tag{A.12}$$

The critical value obtained with this method coincides with that obtained with the theoretical approach presented in this paper when $\boldsymbol{\omega} = \mathbf{n}\delta, \delta \to 0$. The case for $\sigma_{11} = 0$ and $r = 2$, for different values of ϕ and θ, is shown in Fig. A.1 as an example.

The above calculations provide a nontrivial and completely independent verification of the accuracy of our Bloch wave numerical calculations, thus adding confidence in the calculations presented here. It is worth noticing that for the rectangular section selected, where a local buckling mode is the critical one as seen in Fig. 5, the long wavelength mode appears at strains that are at two orders of magnitude higher or more, depending on the orientation $\mathbf{n}$.

Appendix B. Finite element simulations

As an additional method to check the validity of the presented approach, finite element models of the honeycomb cores considered were built in Abaqus/Standard, in order to perform analysis using the BUCKLING command. The models are constructed as a combination of the unit cells described in Section 2.1, with different values of the axial length H, which allows to explore different values of the out-of-plane wavenumber ω_3.

The cell walls were modeled using the S4 general shell/plate element. A regular mesh with square elements was adopted, with a sufficiently small element size to ensure convergence. The boundary conditions applied are such that they ensure that the loading is uniform within all cell walls, while at the same time being periodic in the three directions, in order to approximate an infinite structure. This is achieved using the EQUATION command.

Despite the use of periodic boundary conditions, the FEM model is limited to instabilities that are exactly periodic, and so it is unable to provide the correct value of the buckling load of the infinite structure. It has been used to compare the critical strain of a finite number of cases where the size of the FEM model has been chosen to match the critical eigenmode predictions of the infinite perfect structure; the errors in the predictions of the corresponding models were in these cases lower than 0.1%.

References

Aktay, L., Johnson, A., Kröplin, B., 2008. Numerical modelling of honeycomb core crush behaviour. Eng. Fract. Mech. 75, 2616–2630.

Geymonat, G., Müller, S., Triantafyllidis, N., 1993. Homogenization of nonlinearly elastic materials, microscopic bifurcation and macroscopic loss of rank-one convexity. Arch. Rat. Mech. Anal. 122, 231–290.

Gibson, L., Ashby, M., 1997. Cellular Solids: Structure and Properties. Cambridge University Press. second edition.

Gong, L., Kyriakides, S., Triantafyllidis, N., 2005. On the stability of kelvin cell foams under compressive loads. J. Mech. Phys. Solids 53, 771–794.

Michel, J., 2013. Work in preparation for publication.

Michel, J., Lopez-Pamies, O., Ponte Castañeda, P., Triantafyllidis, N., 2007. Microscopic and macroscopic instabilities in finitely strained porous elastomers. J. Mech. Phys. Solids 55, 900–938.

Michel, J., Lopez-Pamies, O., Ponte Castañeda, P., Triantafyllidis, N., 2010. Microscopic and macroscopic instabilities in finitely strained fiber-reinforced elastomers. J. Mech. Phys. Solids 58, 1776–1803.

Okumura, D., Ohno, N., Noguchi, H., 2002. Post-buckling analysis of elastic honeycombs subject to in-plane biaxial compression. Int. J. Solids Struct. 39, 3387–3503.

Papka, S., Kyriakides, S., 1994. In-plane compressive response and crushing of honeycomb. J. Mech. Phys. Solids 42, 1499–1532.

Papka, S., Kyriakides, S., 1998. Experiments and full-scale numerical simulations of in-plane crushing of a honeycomb. Acta Mater. 46, 2765–2776.

Papka, S., Kyriakides, S., 1999. In-plane biaxial crushing of honeycombs – part ii: analysis. Int. J. Solids Struct. 36, 4397–4423.

Radford, D., McShane, G.J., Deshpande, V., Fleck, N., 2007. Dynamic compressive response of stainless-steel square honeycombs. J. Appl. Mech. 74, 658–667.

Rahtbun, H., Radford, D., Xue, Z., He, M., Yang, J., Deshpande, V., Fleck, N., Hutchinson, J., Zok, F., Evans, A., 2006. Performance of metallic honeycomb-core sandwich beams under shock loading. Int. J. Solids Struct. 43, 1746–1763.

Timoshenko, S.P., Gere, J.M., 1961. Theory of Stability. McGraw-Hill Book Company, second edition.

Triantafyllidis, N., Nestorovic, M.D., Schraad, M.W., 2006. Failure surfaces for finitely strained two-phase periodic solids under arbitrary plane strains. J. Appl. Mech., 73.

Triantafyllidis, N., Schnaidt, W., 1993. Comparison of microscopic and macroscopic instabilites in a class of two-dimensional periodic composites. J. Mech. Phys. Solids 41, 1533–1565.

Triantafyllidis, N., Schraad, M., 1998. Onset of failure in aluminum honeycombs under general in-plane loading. J. Mech. Phys. Solids 46, 1089–1124.

Wilbert, A., Jang, W.Y., Kyriakides, S., Floccari, J., 2011. Buckling and progressive crushing of laterally loaded honeycomb. Int. J. Solids Struct. 48, 803–816.

Yamashita, M., Gotoh, M., 2005. Impact behavior of honeycomb structures with various cell specifications–numerical simulation and experiment. Int. J. Impact Eng. 32, 618–630.

Zhao, H., Gary, G., 1998. Crushing behaviour of aluminium honeycombs under impact loading. Int. J. Impact Eng. 21, 827–836.